






COMMUNICATIONS PHYSICS

ARTICLE

DOI: 10.1038/s42005-018-0091-7

OPEN

2D superconductivity and vortex dynamics in 1T-MoS₂

Chithra H. Sharma ¹, Ananthu P. Surendran¹, Sangeeth S. Varma ² & Madhu Thalakulam ¹

The Berezinskii-Kosterlitz-Thouless phase transition and Bose metal phase, driven by vortices and their dynamics are the hallmark features of a clean two-dimensional superconductor. Materials with a minimal structural disorder and high conductivity are essential for the observation of these features. 1T-MoS₂, a relatively unexplored metallic van der Waals material, is a promising candidate in this regard. Here, we report the observation of two-dimensional superconductivity in a few-layer 1T-MoS₂ device. The electrical characterisation reveals a transition temperature $T_c \sim 920$ mK. Berezinskii-Kosterlitz-Thouless transition and anisotropy in the magneto-transport confirm the dimensionality of the superconductivity. In addition, we observe an enhancement in the parallel upper-critical-field and emergence of the Bose metal state in our sample. The observation of 2D superconductivity in 1T-MoS₂ and the capability to scalably engineer this phase on the semiconducting 2H-MoS₂ phase opens up a new route for the realisation and study of monolithic hybrid quantum circuits.

¹School of Physics, Indian Institute of Science Education and Research, Thiruvananthapuram, Kerala 695551, India. ²BITS-Pilani, K. K. Birla, Goa Campus, Goa 403726, India. Correspondence and requests for materials should be addressed to M.T. (email: madhu@iisertvm.ac.in)

Systems with reduced dimensions provide an opportunity to test fundamental theorems, formulate new ones and access new technologies. The search for non-Abelian quantum Hall systems in one-dimensional constrictions¹ and superconductivity in two-dimensions (2D)^{2,3} are a few examples. Mermin-Wagner theorem forbids ordering and spontaneous symmetry breaking in dimensions $D \leq 2$ for non-zero temperatures⁴. In contrast, experiments involving 2D systems vary; isolation of a single atomic layer of graphite⁵, 2D metallic state at ultra-low-temperatures⁶ and 2D superconductivity³ invoke discussions on the limit and applicability of the theorem to practical systems. Traditionally, 2D systems are realised on interfaces of bulk materials or thin films which are strongly disordered, while controlled experiments in this direction require systems with a minimal structural disorder. The van der Waals (vW) materials, highly crystalline and inherently two-dimensional in the few-layer limit, have recently become one of the most sought-after choices for exploring various quantum phenomena^{7–11}. Among the vW materials, transition metal dichalcogenides (TMDCs), and in particular MoS₂, has shown potential as a platform for observing quantum phenomena and for fabricating quantum devices^{7–12}. Apart from the high degree of electrical tunability, what makes MoS₂ fascinating is the presence of 2D polymorphs displaying a wide spectrum of electrical properties¹³: 2H and 3R are large bandgap semiconductors, 1T⁺ and 1T[−] are narrow bandgap semiconductors and 1T is metallic. The prospect of engineering a 2D superconducting polymorphic phase could make MoS₂ a universal platform for hosting hybrid quantum circuits consisting of semiconducting and superconducting circuit elements^{14–16}. Recently, superconducting phase transition has been reported in 1T and 1T[−] phases of MoS₂^{17–19}, nevertheless the electrical transport is not explored in detail, and the dimensionality of superconductivity is not addressed. 2D superconductivity is limited to systems having sheet-resistance less than the quantum resistance, $R_Q = \frac{h}{4e^2} \sim 6.45$ k Ω ^{3,20}; the metallic nature and high carrier concentration make 1T-MoS₂ a natural choice.

Vortices and their dynamics are characterising features of superconductivity in the 2D limit. The Berezinskii-Kosterlitz-Thouless (BKT) phase transition^{21,22} caused by vortex-antivortex unbinding and the anisotropy in the magneto-transport are considered as the signatures of 2D superconductivity. Systems with a low disorder in the presence of a magnetic field reveal a 2D quantum metallic phase (Bose metal) as a result of dissipation induced by disruption of global phase coherence^{23–27}. Until the advent of vW materials³ 2D superconductivity has been confined to disordered material systems^{20,28–31} such as the interface of bulk materials and thin films. Low structural disorder and high crystallinity make 2D superconductivity and associated phenomena easier to observe in vW systems compared to disordered systems. A substantial increase in the parallel upper critical-field compared to that predicted by the Pauli limit has been observed in crystalline 2D systems^{28,32–35}. This has been attributed to spin-orbit coupling (SOC) and broken-inversion symmetry, resulting in spin-splitting of conduction electrons making it resilient to the magnetic field induced pair breaking. A similar enhancement in the upper critical field has also been reported in centrosymmetric systems recently³⁶.

Owing to the limited electrical tunability, attempts to explore superconductivity in Graphene by doping³⁷ have not met with much success. Many of the transition metal carbides and nitrides exhibit superconductivity in the bulk form³⁸, and 2D superconductivity has been identified in Mo₂C recently³⁹. Among the TMDCs, NbSe₂ and TaS₂ have shown superconductivity in the bulk^{40,41} and also in the 2D limit^{33,42}. Both mono-layer and few-layer NbSe₂ have shown 2D superconductivity with Ising

pairing³³ and emergence of the Bose metallic phase²³. NbSe₂ and TaS₂, being metallic in nature, have limited electrical tunability. In addition, they are prone to oxidation, making device fabrication and integration with other materials challenging^{23,42,43}. Carrier densities $\sim 10^{14}$ cm^{−2} and an insulating-to-superconducting transition have been reported in 2H-MoS₂^{32,44–46}, 2H-MoSe₂⁴⁷, 2H-WSe₂^{34,48} and 1T-SnSe₂⁴⁹ using the ionic-liquid gating technique. Ising pairing has been observed in ionic-liquid gated 2H-MoS₂^{32,45,46} and 2H-WSe₂^{34,48} devices. A summary of important works on 2D superconductivity and associated features are tabulated in Supplementary Table 1.

1T-MoS₂, metallic in nature with a high carrier concentration, meets the resistance requirement to exhibit 2D superconductivity. The 1T phase is generally prepared by structural modification of the 2H phase either by chemical intercalation⁵⁰ or by physical processes such as high-energy electron irradiation or plasma treatment^{51–53}. Stability of the 1T phase is a highly debated topic. Chemically converted 1T-MoS₂ is reported to be unstable against time and temperature making it not suitable for the device fabrication, in contrast to those prepared by physical routes^{52–55}. Scalable and controllable engineering of the 1T phase on the 2H phase has been demonstrated recently⁵³. The possibility of observing 2D superconductivity on the 1T phase can make MoS₂ a potential choice for hosting 2D monolithic hybrid quantum circuits.

In this manuscript, we report the observation of 2D superconductivity, BKT phase transition and the emergence of Bose metallic state in an ~ 8 nm thick (~ 12 layers) 1T-MoS₂ sample. The 1T-MoS₂ samples are prepared from the 2H phase using forming-gas microwave plasma assisted phase engineering. We characterise the 1T phase by high-resolution transmission electron microscopy (HR-TEM). Details of the sample preparation and in-depth structural characterisation can be found elsewhere⁵³. The electrical characterisations consist of low-noise four-probe transport measurements from 300 K down to 4 K and magneto-transport measurements from 4 K down to 12 mK. Current-voltage (I - V) characteristics show excellent linearity down to 4 K without any dependence on the back-gate voltage, suggesting the presence of a metallic state^{13,53} in our sample. The sample resistance shows a sharp drop at a temperature of ~ 1.2 K. The resistance vanishes for lower temperatures signalling a transition to the superconducting state with a $T_c \sim 920$ mK. We confirm the 2D nature of the superconductivity from magneto-transport anisotropy and the presence of the BKT phase transition. Magneto-transport measurements reveal a parallel critical-field manifold of the Pauli limit, possibly due to the presence of high SOC in our system, making it a potential candidate for the realisation of superconducting circuit elements operational at high magnetic fields. The sample also exhibits a transition to Bose metallic state, a signature of a clean 2D superconducting system.

Results

Characterisation of 1T-MoS₂ samples. Figure 1a shows an HR-TEM image with the selected area electron diffraction (SAED) pattern of a representative 1T-MoS₂ sample prepared from the 2H phase by the plasma treatment⁵³. The sample shows extended 1T regions, whose area is primarily limited by the area of the starting 2H flake. The sharp SAED spots are indicative of highly crystalline extended 1T regions in our sample. We also find tiny isolated 2H regions (bounded in green) which we believe are phase transformed back as a result of prolonged exposure to the energetic electron beam. The 1T phase is characterised by octahedral coordination between the Mo and S atoms⁵⁵. Figure 1b shows magnified view of the HR-TEM image of the 1T region while the corresponding atomic arrangement of the Mo and S

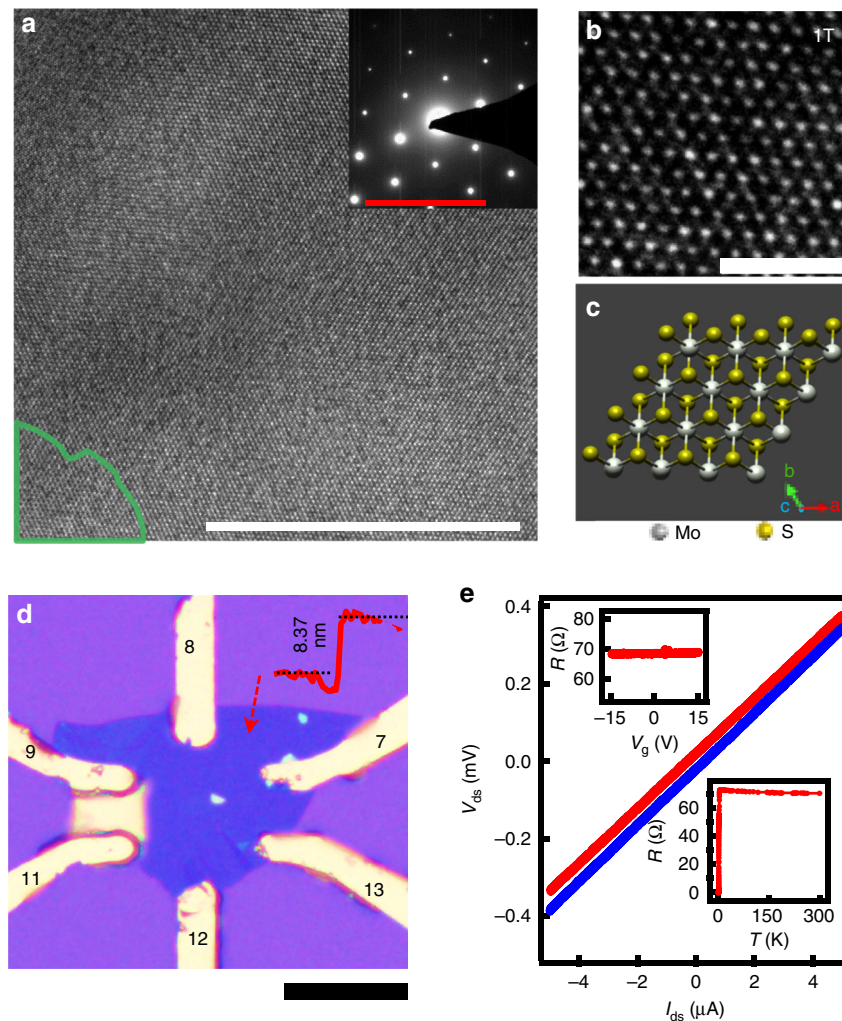


Fig. 1 Basic characterisation of the 1T-MoS₂ samples. **a** HR-TEM image with the diffraction pattern of a plasma treated MoS₂ sample showing the 1T-phase. Area of the 2H-phase is enclosed in green. Scale bar is 20 nm. **b**, **c** Magnified view of the 1T region and the corresponding atomic arrangement, respectively. Scale bar is 2 nm. **d** The optical image of the device with the probes marked. Top-inset: Height profile obtained along the arrowed-line using an atomic force microscope showing a thickness of 8.37 nm. Scale bar is 20 μm. **e** Four-probe *I-V* characteristics of the device at 300 K (red) and 4 K (blue). The traces are offset along the *y*-axis by 20 μV for visibility. Top-inset: four-probe resistance versus back-gate voltage at 300 K, bottom inset: Four-probe resistance versus temperature from 300 K down to 12 mK

atoms is shown Fig. 1c. Mo atoms, by virtue of their superior visibility in the TEM images, appear as bright spots in contrast to S atoms⁵⁶. More details on the sample preparation, structural and electrical characterisation can be found elsewhere⁵³.

The optical image of a 1T-MoS₂ device on a Si/SiO₂ substrate is shown in Fig. 1d. The electrical contacts are defined by photolithography followed by Cr/Au metallisation. We estimate a thickness of ~8 nm (~12 layers) for the 1T-MoS₂ flake using atomic force microscopy (AFM). A height-profile obtained from the AFM along the red-arrowed line is shown in the inset. Figure 1e shows the four-probe *I-V* characteristics of the sample at 300 K (red) and 4 K (blue). We use probes 7, 8, 9 and 13 for all the transport measurements presented in this manuscript. The *I-V* characteristics show excellent linearity both at 300 K (red) and 4 K (blue). The traces are offset along the *y*-axis by 20 μV for better visibility. We observe that the normal state resistance of the sample at 300 K, ~70 Ω, undergoes a slight increase, by ~2 Ω, as the sample is cooled down to 4 K. In addition, the resistance of the sample shows little variation with the back-gate voltage *V_g*, as shown in the top-left inset to Fig. 1e. The linear *I-V* characteristics without any gate-voltage dependence suggest the metallic nature

of the 1T-MoS₂. From the four-probe resistance (~70 Ω) we calculate a sheet resistance *R_s* ~108 Ω/□ for the sample. From the conductivity $\sigma_s = \frac{n_s e^2 \tau}{m^*}$, we obtain $k_F \cdot l = \frac{(\hbar/e^2)}{R_s} \sim 239$ for our sample, which satisfies the Ioffe-Regel criteria⁵⁷, $k_F \cdot l \geq 1$, the disorder limit for metallic conduction. *k_F* is the Fermi wave vector, and *l* is the mean-free-path of electrons in our sample. From the Hall measurements and the sheet resistance, we estimate a carrier concentration of ~2.3 × 10¹⁵ cm⁻² and a mean-free-path *l* ~20 nm.

The resistance as a function of temperature from 300 K down to 12 mK is shown in the lower-right inset of Fig. 1e. A magnified view of the resistance versus temperature in this range is shown in the Supplementary Fig. 1. The resistance shows negligible temperature dependence down to 4 K. This concurs with the fact that our sample consists of continuous 1T regions as inferred from the TEM analysis⁵³. In contrast, transport on 1T-MoS₂ systems prepared by chemical routes has shown strong temperature dependence which has been attributed to hopping or activated behaviour owing to disorder or lower phase purity^{13,58}. As the sample is cooled below 4 K, the resistance

decreases, drops sharply around 1.2 K and vanishes for lower temperatures signalling the presence of a superconducting state. We note here that the carrier concentration of our sample is two-orders higher in magnitude compared to the minimum carrier concentration reported for the observation of 2D superconductivity in ionic-liquid gated MoS₂³². In addition, the sheet resistance of our sample is considerably lower than the quantum resistance, the upper limit to observe 2D superconductivity³.

Anisotropy in magneto-transport. To understand the nature and dimensionality of superconductivity in our device, we explore magneto-transport in the parallel and perpendicular magnetic field orientations. Figure 2a, b show the resistance of the sample versus temperature for various magnetic field values in the parallel and perpendicular orientations, respectively. Figure 2c, d shows the magneto-resistance of the sample for temperatures

between 12 mK and 1.2 K in the parallel and perpendicular magnetic field directions, respectively. The temperature at which the resistance reduces to 50% of the normal state resistance R_N ($\sim 70 \Omega$), at zero magnetic fields, is regarded as the critical temperature T_c . $T_c = 920 \pm 10$ mK for our sample which corresponds to a Bardeen-Cooper-Schrieffer (BCS) energy gap $2\Delta_{BCS} = 3.52K_B T_c \sim 280 \mu\text{eV}$ ⁵⁹. The transition moves to lower temperature values with the magnetic field and eventually vanishes above a critical field B_{c2}^{\parallel} for parallel and B_{c2}^{\perp} for perpendicular orientations. The critical field is estimated as the field at which the resistance of the sample reduces to 50% of R_N . We observe a large anisotropy in the transport with respect to the magnetic field orientations and also a broadening of the transition for the parallel configuration. The broadening of the transition may be caused by phase fluctuations induced by the magnetic field⁶⁰. These observations are atypical of a 3D superconducting state and points towards the presence of a 2D superconducting state in our sample.

For a 2D superconductor, the Tinkham's model predicts the behaviour of critical fields for parallel and perpendicular configurations; $B_{c2}^{\parallel}(T) = \frac{\sqrt{3}\phi_0}{\pi\xi_{GL}(0)d_{sc}} \left(1 - \frac{T}{T_c}\right)^{1/2}$ in the parallel orientation and $B_{c2}^{\perp}(T) = \frac{\phi_0}{2\pi\xi_{GL}(0)^2} \left(1 - \frac{T}{T_c}\right)$ in perpendicular orientation³¹, where ϕ_0 is the flux quantum, $\xi_{GL}(0)$ is the Ginzburg-Landau coherence length and d_{sc} is the effective thickness of the superconductor. Figure 2e shows the dependence of the critical magnetic field on the temperature for parallel (green) and perpendicular (blue) configurations. The green and blue dotted lines are fits using Tinkham's model for the parallel and perpendicular orientations, respectively, showing good agreement with the theory. From the fits, we estimate $\xi_{GL}(0) = 11.9 \pm 2.8$ nm and $d_{sc} = 12.1 \pm 3.1$ nm. The BCS coherence length, $1.35 \xi_{GL}(0) < l$ implies that our device can be regarded as a clean superconductor. The estimated superconducting thickness obtained from the fit is of the same order but slightly larger than the sample thickness measured by AFM; similar discrepancies have been reported in the past^{23,31}. We note here that in the parallel field configuration the critical field is highly sensitive to small angular deviations in the sample orientation which may also contribute to this error⁵⁹.

The Pauli limit⁵⁹ described by the BCS theory put an upper bound to $B_{c2}^{\parallel}(0) = 1.86 T_c$ in 2D superconductors. In our sample, the measured B_{c2}^{\parallel} at 12 mK is $\sim 6.25 T$, \sim four-times the value $1.618 T$ predicted by the Pauli limit. A similar enhancement in the B_{c2}^{\parallel} has been observed in systems with high SOC (i) TMDC superconductors in the monolayer limit owing to Ising pairing of electrons³²⁻³⁴ (ii) crystalline thin-film superconductors with high SOC and substrate-induced symmetry breaking²⁸ (iii) recently in centrosymmetric few layer TMDCs³⁶. This has been suggested due to the SOC induced spin splitting of conduction electrons making pair breaking unfavourable under an external magnetic field; further studies are required to understand the detailed mechanism.

The Berezinskii-Kosterlitz-Thouless transition. A superconducting state is characterised by a critical current I_c , above which the material turns normal⁵⁹. Figure 3a shows the I - V characteristics from 12 mK (blue) to 4 K (red) at zero magnetic fields. A plot of I_c versus temperature is shown in the inset. We observe that as the I_c reduces with temperature and finally becomes zero as the normal state is reached. Dynamics of vortices leave a clear signature in the transport characteristics. In a 2D superconductor, in the absence of a magnetic field, the transition to zero resistance as the sample is cooled involves (i) formation of

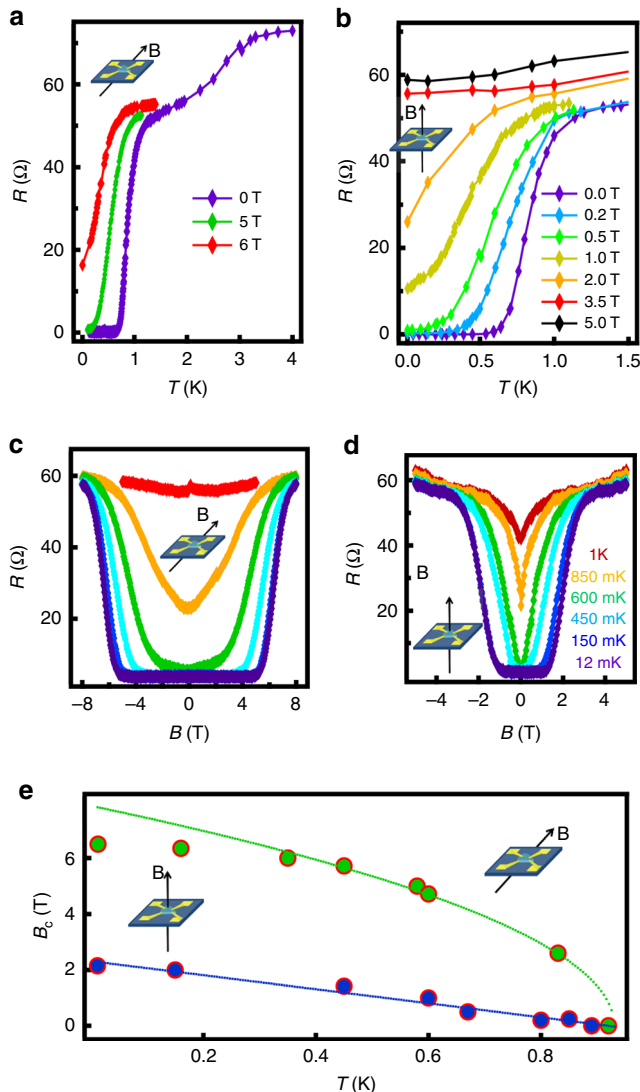


Fig. 2 Magneto-transport in the superconducting transition regime. **a** Sample resistance versus temperature for parallel magnetic fields in the superconducting transition region. **b** The resistance versus temperature at different magnetic fields in the perpendicular orientation. **c, d** The Magneto-resistance at different temperatures between 12 mK and 1 K with the magnetic field in parallel (**c**) and perpendicular (**d**) orientations. **e** Critical field versus temperature for parallel (green) and perpendicular (blue) orientations. The dotted lines show fit to the Tinkham's model

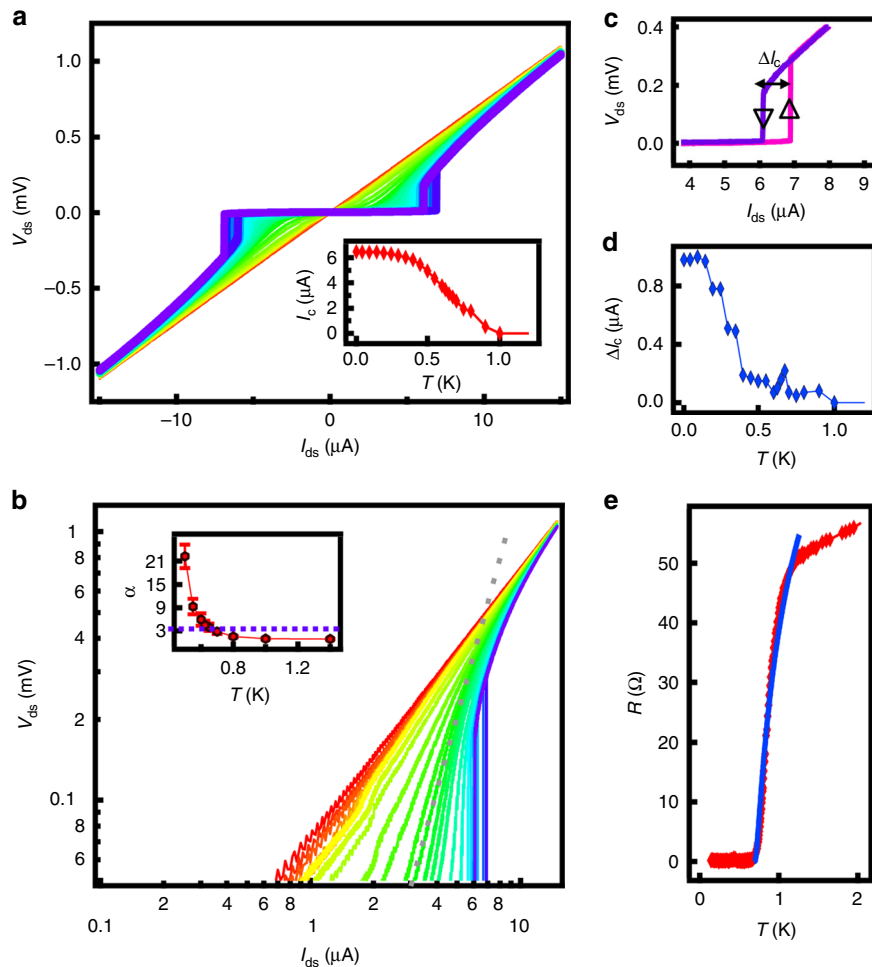


Fig. 3 Current-Voltage (I - V) characteristics and Berezinskii-Kosterlitz-Thouless transition. **a** The I - V characteristics for temperatures 12 mK (blue) to 4 K (red) at 0 T. Inset: The plot of critical current versus temperature. **b** The I - V plot in the log scale showing the power law behaviour $V \propto I^{\alpha(T)}$, where the grey dotted line corresponds to $\alpha=3$ at a temperature ~ 0.675 K corresponding to the Berezinskii-Kosterlitz-Thouless transition. The inset shows the value of the scaling exponent, $\alpha(T)$ versus temperature. The error-bar corresponds to the standard deviation of the fit **(c)** Magnified view of the I - V characteristics at 12 mK showing hysteresis with sweep direction **(d)** Plot of hysteresis in I_c versus temperature **(e)** Plot of Resistance versus temperature at 0 T where the blue line shows fit to the Halperin-Nelson equation, giving an estimate of $T_{\text{BKT}} = 0.689$ K

Cooper-pairs at T_c (ii) vortex-antivortex pairing reducing dissipation (the BKT transition at T_{BKT}) and (iii) the condensation of the Cooper pairs into a single state resulting in the vanishing of the resistance for still lower temperatures. The BKT phase transition is a hallmark phenomenon of 2D superconductivity^{22,61}. A signature of the BKT transition is the deviation from the linear nature of the I - V characteristics in the normal state to a power-law dependence $V \propto I^{\alpha(T)}$ obeying Halperin-Nelson scaling as a result of the motion of the free vortices in the system; the exponent $\alpha(T)$ takes a critical value of 3 at the transition^{23,39,61}. Figure 3b shows the log-log scale plot of the I - V characteristics in the vicinity of the superconducting transition exhibiting the power law dependence. The inset shows a plot of the scaling exponent $\alpha(T)$ versus temperature as the sample undergoes a transition from the normal to the superconducting state. As the temperature is lowered, the slope α increases from unity corresponding to the Ohmic behaviour and diverges rapidly around $\alpha = 3$. The grey dotted line in the main panel, and the purple dotted-line in the inset corresponds to $\alpha = 3$; the corresponding temperature is the BKT transition temperature $T_{\text{BKT}} \sim 675$ mK.

We observe hysteresis in the I - V traces between forward and reverse current sweeping directions in the superconducting state as shown in Fig. 3c. This is regarded as another sign of the

presence of vortex-antivortex pairs in the system^{23,62}. Above T_{BKT} the free vortices are stable, and the correlations between distant pairs are destroyed. Below T_{BKT} the free vortices created as a result of the driving current also pair-up, and the voltage developed due to the vortex motion in the unbound state causes the hysteresis in the critical current ΔI_c ^{62,63}. ΔI_c as a function of temperature is shown in Fig. 3d. The hysteresis reduces with temperature and disappears around 675 mK which corresponds to the T_{BKT} estimated from the I - V characteristics using the scaling theory.

According to the Halperin-Nelson equation^{64,65}, the resistance in a 2D superconductor in the vicinity of the transition varies as $\exp\left(-b(T - T_{\text{BKT}})^{-\frac{1}{2}}\right)$. A plot of resistance versus temperature with the fit to the equation (blue line) is shown in Fig. 3e. We extract a value of 689 ± 7 mK for T_{BKT} from the fit. This value is consistent with the T_{BKT} , ~ 675 mK, estimated from the I - V curves (using both the scaling law and the hysteresis data shown in Fig. 3d).

The emergence of the Bose metal phase. A strongly disordered 2D superconductor makes a transition to an insulating state under the application of a perpendicular magnetic field²⁵. In

contrast, systems with a low disorder have shown a quantum phase transition to an intermediate 2D metallic state, Bose metal, with a resistance much lower than R_N ^{23,66}. This state is characterised by a saturation of the resistance as $T \rightarrow 0$. Besides, the resistance obeys a power law with the magnetic field^{23,66,67}. These observations have been theoretically addressed using various Bosonic models^{25–27}. Disruption of the global phase coherence is considered as the key to this dissipation. Das and Doniach, using the Bose-Hubbard model attribute this to the dynamical gauge field fluctuations^{24,25}. Phillips and Dalidovich model the system as a glassy phase-landscape making the motion of Bosonic charge carriers dissipative^{26,27}.

Arrhenius plot of resistance for perpendicular magnetic fields below B_{c2}^\perp shown in Fig. 4a display the existence of Bose metal phase in our sample. Though a sharp drop in the resistance is observed at the superconducting transition point, the system does not exhibit a zero-resistance state for finite field values and saturates to small values compared to R_N as the temperature is lowered. The resistance exhibits an activated behaviour for temperatures close to T_c due to temperature-driven depairing of vortex-antivortex pairs. The pair dissociation energy $U(B)$ is obtained from the fit to Fig. 4a using $R \propto \exp\left(-\frac{U(B)}{T}\right)$ ²³ in the activated transport region. Figure 4b shows a plot of $U(B)$ hence obtained versus the magnetic field with a fit to the equation $U(B) = U_0 \ln(B_0/B)$ ²³, shown in blue. From the fit, we obtain $U_0 = 1.18$ K $\sim 1.76 T_{\text{BKT}}$ and $B_0 = 1.359$ T $\sim B_{c2}^\perp$. The crossover

temperature from the activated transport behaviour to the resistance-saturation and the activation energy reduces with the magnetic field ruling out the possibility of the state being an artefact of sample heating⁶⁸. The sample is protected from the electrical noise and radiation using extensive filtering and radiation shields installed at various temperature stages of the measurement system, details of which can be found in the methods section.

The superconductor to the Bose metal transition is characterised by a resistance scaling $R \propto (B - B_{c0})^{2\nu}$ where $B_c(0)$ is the critical field for the superconductor to Bose metal transition and ν is the exponent by which the superfluid correlation length diverges^{23,25,26}. Figure 4c is a log-log scale plot of resistance versus perpendicular magnetic field for temperatures below T_{BKT} with a fit to the above equation. A plot of the scaling exponent 2ν extracted from the fit versus temperature is shown in the inset. The exponent assumes a value of unity near T_{BKT} corresponding to a linear behaviour and grows nonlinear as the temperature is reduced with $2\nu = 2.37 \pm 0.16$ for lower temperatures. We note that the exponent has been shown to vary with sample thickness and the value of the exponent we obtained is comparable to those observed elsewhere for similar systems²³.

Figure 4d shows the B - T phase diagram displaying different regimes of transport arising due to vortex dynamics. The B_{c2}^\perp versus T data shown in red-dots extracted from the magneto-transport measurements separate these phases from the normal state. As the temperature is lowered below T_c , the system goes into a thermally activated flux flow (TAFF) regime^{20,23}, shaded in blue. The 2D superconducting phase (2DS) with vanishing resistance, shown in green, exists only at sufficiently low temperatures and magnetic fields. The Bose metal (BM) state characterised by finite dissipation at higher magnetic field values is shown in purple. The cross-over from the thermally activated transport to a resistance saturation, shown in blue squares, defines the boundary between the TAFF and the BM regimes. The 2DS state shows a hysteresis in the I - V characteristics and the vanishing of this hysteretic behaviour defines the boundary²³.

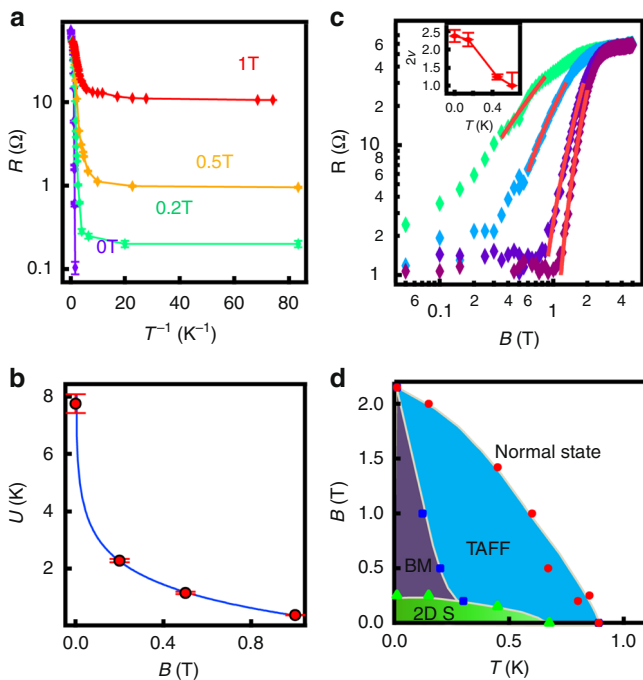


Fig. 4 Bose metal (a) Arrhenius plot of resistance versus temperature for various perpendicular magnetic fields. The error-bar corresponds to the resolution in the resistance measurements that is restricted by the noise floor of the voltage amplifier. (b) The red dots are the vortex binding energy calculated from the linear region in (a), and the blue line shows the fit to equation $U(B) = U_0 \ln(B_0/B)$. The error-bar corresponds to the standard deviation of the fit. (c) The magneto-resistance plot for the perpendicular magnetic field in log-scale. The solid red lines on the traces are fit to the scaling relation $R \propto (B - B_{c0})^{2\nu}$. A plot of 2ν versus temperature is given in the inset. The error-bar corresponds to the standard deviation of the fit. (d) H - T Phase diagram showing different regimes of transport in the system; normal, thermally activated flux flow (TAFF), Bose metal (BM), and the 2D superconductor (2DS)

Discussion

In this manuscript, we explored 2D superconductivity in a large area few-layer 1T-MoS₂ sample. We investigated the transport properties of the sample from 300 K down to 4 K in a closed cycle cryostat and from 4 K down to 12 mK in a dilution refrigerator. The carrier concentration of $\sim 2.3 \times 10^{15}$ cm⁻² and a sheet resistivity of ~ 108 Ω/□ put the sample in the clean metallic regime. In addition, the linear I - V characteristics with no dependence on the back-gate voltage underline metallic conduction in our sample. Below a temperature of ~ 1.2 K, the sample undergoes a superconducting transition with a $T_c \sim 920$ mK. We observe a clear anisotropy in the magneto-transport obeying Tinkham's model. The superconductivity in our sample is accompanied by the BKT phase transition, enhanced parallel critical-field and a transition to the Bose metal state, which are characteristic features of a clean 2D superconducting system. The BKT transition is identified from the exponential scaling of the I - V characteristics, hysteresis in the critical current and also from resistance versus temperature characteristics obeying the Halperin-Nelson equation. The sample undergoes a transition from the superconducting to a 2D quantum metallic state, the Bose metal, under the application of a perpendicular magnetic field. Such behaviour is generally observed in systems with low disorder density. In addition, we observed a manifold increase in the parallel upper critical field beyond the Pauli limit possibly due to high SOC in our sample.

The metallic 1T-MoS₂ is a widely studied system from the materials point of view, though, lacks in-depth electrical characterisations for device applications. We believe this work will add depth to the current understanding of the nature of transport in the system. The enhanced upper critical-field, even in the multilayer regime, makes 1T-MoS₂ a potential system for on-chip superconducting circuit elements and cavity QED applications requiring operation at higher external magnetic fields. The possibility of scalably and controllably engineering the 2D superconducting 1T phase on the semiconducting 2H phase opens up a new landscape for hybrid quantum device circuits.

Methods

Device fabrication. MoS₂ samples commercially procured from SPI supplies are exfoliated and transferred onto a clean Si wafer hosting 300 nm SiO₂ layer. The 2H to 1T phase conversion is achieved by exposing the exfoliated samples to forming-gas (90% Ar + 10% H₂) microwave plasma. The details of the plasma system and the 1T conversion process can be found elsewhere⁵³. Contacts on the 1T samples are made by standard photolithography followed by Cr/Au metallisation.

Low-noise transport measurements. Low-noise transport measurements are performed in a cryogen-free dilution refrigerator equipped with a superconducting magnet and also in a closed cycle 4 K cryo-cooler. The measurement setup consists of various filtering circuits and radiation shields at different temperature stages to minimise the electrical noise on the sample. The sample is shielded from external radiation using metallic shields attached successively on various temperature stages; 10 mK (mixing chamber), 700 mK (Still), 3.5 K (superconducting magnet), 50 K and 300 K (room temperature flange). Outside the cryostat, the measurements wires are Faraday shielded from any ambient radiation using metallic enclosures and shielded cables. The circuit consists of low-pass π -filters and RC filters at room temperature, low-pass RC filter at 10 mK (mixing chamber) and a high-frequency copper-powder filter⁶⁹ at 10 mK (mixing chamber). The cumulative cut-off frequency (-3 dB) for all the measurement lines is ~ 1.4 kHz. The attenuation for all signals around 10 kHz is ~ 40 dB and above 1 GHz exceeds ~ 60 dB. In addition, a dedicated low-noise earthing arrangement is used to define the ground points for the entire measurement system.

Data availability:

All data generated or analysed during this study are included in this published article and its supplementary information files.

Received: 21 June 2018 Accepted: 6 November 2018

Published online: 07 December 2018

References

- Radu, I. P. et al. Quasi-particle properties from tunneling in the $\nu = 5/2$ fractional quantum hall state. *Science* **320**, 899–902 (2008).
- Weitering, H. H. & Wu, J. Z. Superconductivity: how the unconventional became the new norm. *Supercond. Sci. Technol.* **30**, 040301 (2017).
- Saito, Y., Nojima, T. & Iwasa, Y. Highly crystalline 2D superconductors. *Nat. Rev. Mater.* **2**, 16094 (2016).
- Mermin, N. D. & Wagner, H. Absence of ferromagnetism or antiferromagnetism in one-dimensional or two-dimensional isotropic Heisenberg models. *Phys. Rev. Lett.* **17**, 1133–1136 (1966).
- Novoselov, K. S. et al. Two-dimensional atomic crystals. *Proc. Natl Acad. Sci. USA* **102**, 10451–10453 (2005).
- Eley, S., Gopalakrishnan, S., Goldbart, P. M. & Mason, N. Approaching zero-temperature metallic states in mesoscopic superconductor-normal-superconductor arrays. *Nat. Phys.* **8**, 59–62 (2012).
- Cui, X. et al. Multi-terminal transport measurements of MoS₂ using a van der Waals heterostructure device platform. *Nat. Nanotechnol.* **10**, 534–540 (2015).
- Pisoni, R. et al. Gate-defined one-dimensional channel and broken symmetry states in MoS₂ van der Waals heterostructures. *Nano Lett.* **17**, 5008–5011 (2017).
- Wang, K. et al. Electrical control of charged carriers and excitons in atomically thin materials. *Nat. Nanotechnol.* **13**, 128–132 (2018).
- Lee, K., Kulkarni, G. & Zhong, Z. Coulomb blockade in monolayer MoS₂ single electron transistor. *Nanoscale* **8**, 7755–7760 (2016).
- Neal, A. T., Liu, H., Gu, J. & Ye, P. D. Magneto-transport in MoS₂: Phase Coherence, Spin–Orbit Scattering, and the Hall Factor. *ACS Nano* **7**, 7077–7082 (2013).
- Sharma, C. H. & Thalakulam, M. Split-gated point-contact for electrostatic confinement of transport in MoS₂/h-BN hybrid structures. *Sci. Rep.* **7**, 735 (2017).
- Kim, J. S. et al. Electrical transport properties of polymorphic MoS₂. *ACS Nano* **10**, 7500–7506 (2016).
- Yabuki, N. et al. Supercurrent in van der Waals Josephson junction. *Nat. Commun.* **7**, 10616 (2016).
- Guo, C. et al. Strong coupling of a single photon to a superconducting qubit using circuit quantum electrodynamics. *Nature* **431**, 162–167 (2004).
- Mi, X. et al. A coherent spin-photon interface in silicon. *Nature* **555**, 599–603 (2018).
- Guo, C. et al. Observation of superconductivity in 1T'-MoS₂ nanosheets. *J. Mater. Chem. C* **5**, 10855–10860 (2017).
- Zhang, R. et al. Superconductivity in potassium-doped metallic polymorphs of MoS₂. *Nano Lett.* **16**, 629–636 (2016).
- Fang, Y. et al. Structure re-determination and superconductivity observation of bulk 1T MoS₂. *Angew. Chem.* **57**, 1232–1235 (2018).
- Saito, Y., Kasahara, Y., Ye, J., Iwasa, Y. & Nojima, T. Metallic ground state in an ion-gated two-dimensional superconductor. *Science* **350**, 409–413 (2015).
- Kosterlitz, J. M. & Thouless, D. J. Ordering, metastability and phase transitions in two-dimensional systems. *J. Phys. C* **6**, 1181–1203 (2002).
- Beasley, M. R., Mooij, J. E. & Orlando, T. P. Possibility of vortex-antivortex pair dissociation in two-dimensional superconductors. *Phys. Rev. Lett.* **42**, 1165–1168 (1979).
- Tsen, A. W. et al. Nature of the quantum metal in a two-dimensional crystalline superconductor. *Nat. Phys.* **12**, 208–212 (2016).
- Das, D. & Doniach, S. Existence of a Bose metal at $T=0$. *Phys. Rev. B* **60**, 1261–1275 (1999).
- Das, D. & Doniach, S. Bose metal: gauge-field fluctuations and scaling for field-tuned quantum phase transitions. *Phys. Rev. B* **64**, 134511 (2001).
- Dalidovich, D. & Phillips, P. Phase glass is a Bose metal: a new conducting state in two dimensions. *Phys. Rev. Lett.* **89**, 027001 (2002).
- Phillips, P. & Dalidovich, D. The elusive Bose metal. *Science* **302**, 243–247 (2003).
- Nam, H. et al. Ultrathin two-dimensional superconductivity with strong spin-orbit coupling. *Proc. Natl Acad. Sci. USA* **113**, 10513–10517 (2016).
- Qin, S., Kim, J., Niu, Q. & Shih, C.-K. Superconductivity at the two-dimensional limit. *Science* **324**, 1314–1317 (2009).
- Jeffrey Gardner, H. et al. Enhancement of superconductivity by a parallel magnetic field in two-dimensional superconductors. *Nat. Phys.* **7**, 895–900 (2011).
- Kim, M., Kozuka, Y., Bell, C., Hikita, Y. & Hwang, H. Y. Intrinsic spin-orbit coupling in superconducting δ -doped SrTiO₃ heterostructures. *Phys. Rev. B* **86**, 085121 (2012).
- Lu, J. M. et al. Evidence for two-dimensional Ising superconductivity in gated MoS₂. *Science* **350**, 1353–1357 (2015).
- Xi, X. et al. Ising pairing in superconducting NbSe₂ atomic layers. *Nat. Phys.* **12**, 139–143 (2016).
- Lu, J. et al. Full superconducting dome of strong Ising protection in gated monolayer WS₂. *Proc. Natl Acad. Sci. USA* **115**, 3551–3556 (2018).
- Saito, Y. et al. Superconductivity protected by spin–valley locking in ion-gated MoS₂. *Nat. Phys.* **12**, 144–149 (2016).
- Cui, J. et al. Transport evidence of Ising superconductivity in few-layer 1Td-MoTe₂. Preprint at <https://arxiv.org/abs/1801.06955> (2018)
- Xue, M. et al. Superconductivity in potassium-doped few-layer graphene. *J. Am. Chem. Soc.* **134**, 6536–6539 (2012).
- Hardy, G. F. & Hulm, J. K. The superconductivity of some transition metal compounds. *Phys. Rev.* **93**, 1004–1016 (1954).
- Xu, C. et al. Large-area high-quality 2D ultrathin Mo₂C superconducting crystals. *Nat. Mater.* **14**, 1135–1141 (2015).
- Revilinsky, E., Spiering, G. A. & Beerntsen, D. J. Superconductivity in the niobium-selenium system. *J. Phys. Chem. Solids* **26**, 1029–1034 (1965).
- Sipos, B. et al. From Mott state to superconductivity in 1T-TaS₂. *Nat. Mater.* **7**, 960–965 (2008).
- Navarro-Moratalla, E. et al. Enhanced superconductivity in atomically thin TaS₂. *Nat. Commun.* **7**, 11043 (2016).
- Cao, Y. et al. Quality heterostructures from two-dimensional crystals unstable in air by their assembly in inert atmosphere. *Nano Lett.* **15**, 4914–4921 (2015).
- Costanzo, D., Jo, S., Berger, H. & Morpurgo, A. F. Gate-induced superconductivity in atomically thin MoS₂ crystals. *Nat. Nanotechnol.* **11**, 339–344 (2016).
- Taniguchi, K., Matsumoto, A., Shimotani, H. & Takagi, H. Electric-field-induced superconductivity at 9.4 K in a layered transition metal disulphide MoS₂. *Appl. Phys. Lett.* **101**, 042603 (2012).
- Ye, J. T. et al. Superconducting dome in a gate-tuned band insulator. *Science* **338**, 1193–1196 (2012).
- Shi, W. et al. Superconductivity series in transition metal dichalcogenides by ionic gating. *Sci. Rep.* **5**, 12534 (2015).

48. Jo, S., Costanzo, D., Berger, H. & Morpurgo, A. F. Electrostatically induced superconductivity at the surface of WS_2 . *Nano Lett.* **15**, 1197–1202 (2015).
49. Zeng, J. et al. Gate-induced interfacial superconductivity in 1T- SnSe_2 . *Nano Lett.* **18**, 1410–1415 (2018).
50. Kappera, R. et al. Phase-engineered low-resistance contacts for ultrathin MoS_2 transistors. *Nat. Mater.* **13**, 1128–1134 (2014).
51. Lin, Y.-C., Dumcenco, D. O., Huang, Y.-S. & Suenaga, K. Atomic mechanism of the semiconducting-to-metallic phase transition in single-layered MoS_2 . *Nat. Nanotechnol.* **9**, 391–396 (2014).
52. Zhu, J. et al. Argon plasma induced phase transition in monolayer MoS_2 . *J. Am. Chem. Soc.* **139**, 10216–10219 (2017).
53. Sharma, C. H., Surendran, A. P., Varghese, A. & Thalakulam, M. Stable and scalable 1T MoS_2 with low temperature-coefficient of resistance. *Sci. Rep.* **8**, 3055 (2018).
54. Pal, B. et al. Chemically exfoliated MoS_2 layers: spectroscopic evidence for the semiconducting nature of the dominant trigonal metastable phase. *Phys. Rev. B* **96**, 195426 (2017).
55. Jiménez Sandoval, S., Yang, D., Frindt, R. F. & Irwin, J. C. Raman study and lattice dynamics of single molecular layers of MoS_2 . *Phys. Rev. B* **44**, 3955–3962 (1991).
56. Lin, Y.-C. et al. Properties of individual dopant atoms in single-layer MoS_2 : atomic structure, migration, and enhanced reactivity. *Adv. Mater.* **26**, 2857–2861 (2014).
57. Fiory, A. T. & Hebard, A. F. Electron mobility, conductivity, and superconductivity near the metal-insulator transition. *Phys. Rev. Lett.* **52**, 2057–2060 (1984).
58. Qiu, H. et al. Hopping transport through defect-induced localized states in molybdenum disulphide. *Nat. Commun.* **4**, 2642 (2016).
59. Tinkham, M. *Introduction to Superconductivity; 2nd edn.* (Dover, 2004).
60. Saito, Y., Nojima, T. & Iwasa, Y. Gate-induced superconductivity in two-dimensional atomic crystals. *Supercond. Sci. Technol.* **29**, 093001 (2016).
61. Mooij, J. E. in *Advances in Superconductivity NATO Advanced Science Institute Series (Series-B: Physics)* (Deaver, B. & Ruvalds, J. eds.) (Springer, US, 1983).
62. Coleman, C. & Bhattacharyya, S. Possible observation of the Berezinskii-Kosterlitz-Thouless transition in boron-doped diamond films. *AIP Adv.* **7**, 115119 (2017).
63. Zybtev, S. G. et al. Switching and Hysteresis on the I-V Curves of Submicron BSCCO (2212) Bridges. *J. Low Temp. Phys.* **139**, 281–288 (2005).
64. Halperin, B. I. & Nelson, D. R. Resistive transition in superconducting films. *J. Low Temp. Phys.* **36**, 599–616 (1979).
65. Lin, Y.-H., Nelson, J. & Goldman, A. M. Suppression of the Berezinskii-Kosterlitz-Thouless transition in 2D superconductors by macroscopic quantum tunneling. *Phys. Rev. Lett.* **109**, 017002 (2012).
66. Saito, Y., Nojima, T. & Iwasa, Y. Quantum phase transitions in highly crystalline two-dimensional superconductors. *Nat. Commun.* **9**, 778 (2018).
67. Christiansen, C., Hernandez, L. M. & Goldman, A. M. Evidence of collective charge behavior in the insulating state of ultrathin films of superconducting metals. *Phys. Rev. Lett.* **88**, 037004 (2002).
68. Phillips, P. W. Not just a phase. *Nat. Phys.* **12**, 206–207 (2016).
69. Bladh, K. et al. Comparison of cryogenic filters for use in single electronics experiments. *Rev. Sci. Instrum.* **74**, 1323–1327 (2003).

Acknowledgements

The authors acknowledge IISER Thiruvananthapuram for the infrastructure and experimental facilities and Anil Shaji for in-depth discussions and critical reading of the manuscript. M.T. acknowledges the funding received from the DST-SERB extramural program (SB/S2/CMP-008/2014). C.H.S. acknowledges CSIR and A.P.S. acknowledges INSPIRE for the fellowship.

Author contributions

M.T. conceived the problem. A.P.S. prepared the samples and performed the structural characterisations. C.H.S. and A.P.S. fabricated the device, C.H.S. performed the transport measurements and analysed the data, C.H.S., S.S.V. designed the data acquisition system and, C.H.S. and M.T. co-wrote the manuscript.

Additional information

Supplementary information accompanies this paper at <https://doi.org/10.1038/s42005-018-0091-7>.

Competing interests: The authors declare no competing interests.

Reprints and permission information is available online at <http://npg.nature.com/reprintsandpermissions/>

Publisher's note: Springer Nature remains neutral with regard to jurisdictional claims in published maps and institutional affiliations.



Open Access This article is licensed under a Creative Commons Attribution 4.0 International License, which permits use, sharing, adaptation, distribution and reproduction in any medium or format, as long as you give appropriate credit to the original author(s) and the source, provide a link to the Creative Commons license, and indicate if changes were made. The images or other third party material in this article are included in the article's Creative Commons license, unless indicated otherwise in a credit line to the material. If material is not included in the article's Creative Commons license and your intended use is not permitted by statutory regulation or exceeds the permitted use, you will need to obtain permission directly from the copyright holder. To view a copy of this license, visit <http://creativecommons.org/licenses/by/4.0/>.

© The Author(s) 2018